1   **Development of a yeast whole-cell biocatalyst for MHET conversion into terephthalic acid**

2   **and ethylene glycol**

3

4

5   Raphael Loll-Krippleber[1,2,*], Victoria Sajtovich[1,2], Michael W. Ferguson[1,2], Brandon Ho[1,2],

6   Brandon J. Payliss[2], Joseph Bellissimo[1,2], Sydney Peters[1,2], Haley D. M. Wyatt[2], & Grant W.

7   Brown[1,2,*]

8

9   [1] Donnelly Centre for Cellular and Biomolecular Research, University of Toronto

10   [2] Department of Biochemistry, University of Toronto

11

12   [*] Corresponding authors

13   raphael.loll.krippleber@utoronto.ca

14   grant.brown@utoronto.ca

15

16

17

18

19

20

21

22

23

Abstract

Background. Over the 70 years since the introduction of plastic into everyday items, plastic waste has become an increasing problem. With over 360 million tonnes of plastics produced every year, solutions for plastic recycling and plastic waste reduction are sorely needed. Recently, multiple enzymes capable of degrading PET (polyethylene teraphthalate) plastic have been identified and engineered. In particular, the enzymes PETase and MHETase from *Ideonella sakaiensis* depolymerize PET into the two building blocks used for its synthesis, ethylene glycol (EG) and terephthalic acid (TPA). Importantly, EG and TPA can be re-used for PET synthesis allowing complete and sustainable PET recycling.

Results. In this study, we used *Saccharomyces cerevisiae* as a platform to develop a whole-cell catalyst expressing the MHETase enzyme, which converts MHET (monohydroxyethyl terephthalate) into TPA and EG. We assessed six expression architectures and identified those resulting in efficient MHETase expression on the yeast cell surface. We show that the MHETase whole-cell catalyst has activity comparable to recombinant MHETase purified from *Escherichia coli*. Finally, we demonstrate that surface displayed MHETase is stable to pH, temperature, and for at least 12 days at room temperature.

Conclusions. We demonstrate the feasibility of using *S. cerevisiae* as a platform for the expression and surface display of PET degrading enzymes and predict that the whole-cell catalyst will viable alternatives to protein purification-based approaches for plastic degradation.

2

Background

Since its invention over 70 years ago, plastic has become a major material for a wide range of items ranging from electronics components to clothing and packaging. It is currently estimated that over 360 million metric tonnes of plastics are produced every year [1,2]. In particular, the ease of production, cheap cost, and material versatility has made polyethylene terephthalate (PET) one of the most abundant plastics globally, with over 56 million metric tonnes produced every year, mainly for use in food packaging and textile fibers [1]. PET is easily produced by esterification of the petrochemicals ethylene glycol and terephthalic acid leading to the formation of polymers which can be easily molded into shape via melting processing, a process invented in the 1970's [3].

Despite the enormous production of PET plastic, current solutions for waste management are lacking and it is estimated that at least 70% of total plastic is found as waste [1]. Two limitations account for the lack of effective plastic recycling solutions. First, recycling technologies for PET via physical or chemical processes leads to loss of material cohesion. Second, the current physical- and/or chemical-based methods of plastic recycling are not energy efficient as they often involve high temperatures and high pressures and often lead to the formation of hazardous by products, making them incompatible with environmentally conscious recycling approaches [1]. In addition, an increasing number of studies have shed light on the impact of plastic waste on animal and human health. Micro- and nano-plastics accumulate in animals from mollusc species to humans [4–6]. Although the physiological effects of these particles remain to be fully understood, recent studies suggest negative effects on biological functions such as oyster reproduction and hepatic lipid metabolism in mice [7,8]. Therefore, new methods for plastic waste management, remediation, and recycling are urgently needed.

70   Recently, enzymes capable of degrading PET plastic have been identified and

71   engineered. In particular, the enzymes PETase and MHETase from the bacteria *Ideonella*

72   *sakaiensis*, isolated from PET-polluted environmental samples, depolymerize PET into the two

73   building blocks used for its synthesis, ethylene glycol (EG) and terephthalic acid (TPA) [9,10].

74   Importantly, EG and TPA obtained via enzymatic hydrolysis can be re-used for PET synthesis

75   allowing complete and sustainable PET recycling [11,12].

76   Much current work has focused on improving PETase through protein engineering.

77   Computational redesign of PETase has led to the development of thermostable variants of this

78   mesophilic enzyme that are active at temperature close to the glass transition of PET, which

79   increases polymer chain mobility to promote access to the ester linkages by the enzyme

80   [11,13,14]. One recent and notable example of such approaches led to the identification of a new

81   variant of PETase, dubbed FAST-PETase, containing 4 thermo-stabilizing mutations, boosting

82   degradation efficiency up to 30-fold, and allowing degradation of entire post-consumer plastic

83   containers in a matter of days [11]. Other studies have focused on identifying other PET

84   degrading enzymes. Most examples involve enzymes from the cutinase, esterase and lipase

85   families and were identified in bacteria and fungi. TfH (lipase), LCC, PHL7, HiC and Thc_Cut2

86   (cutinases) are among the other most promising PET-degrading enzymes and have been

87   extensively characterized and engineered [12,15–19]. Although most of the research efforts have

88   been focused on enzyme identification and enzyme engineering for use in the context of

89   industrial processes using purified enzyme, microbe engineering for PET degradation and

90   remediation has also been conducted. Heterologous expression of PET-degrading enzymes has

91   been achieved in bacteria, yeast, and microalgae [20]. *Pseudomonas putida* has been extensively

92   studied for PET degradation due to its ability to use EG as carbon source as well as for upcycling

93   of TPA into higher value chemicals such as biodegradable plastics [21,22]. Other examples of

94   TPA upcycling include conversion into catechol, muconic acid, glycolic acid, and vanillic acid

95   [23,24]. More recently, *Pichia pastoris* was shown to be a suitable platform for expression of

96   PETase and *Yarrowia lypolitica* was shown to naturally degrade PET and metabolize EG and

97   TPA [25–28].

98   Despite the focus on PETase, MHETase is also a critical component of the enzymatic

99   PET degradation process and is essential for converting the monohydroxyethyl terephthalate

100   (MHET) product of the PETase reaction into TPA and EG. The PETase reaction products consist

101   mainly of MHET, with TPA produced in small quantities if PETase is expressed alone [9].

102   MHET accumulation inhibits PET-hydrolysing enzymes [29,30] reducing their effectiveness,

103   whereas dual systems such as fusion of PETase and MHETase improve PET hydrolysis [31].

104   Consequently, biological systems for MHETase expression and engineering are needed.

105   In this study, we establish a system to express MHETase from *Ideonella sakaiensis* on

106   the surface of the yeast *Saccharomyces cerevisiae*. The resulting whole-cell biocatalyst allows

107   conversion of MHET generated by PETase into TPA and EG (Figure 1A). We surveyed six

108   potential surface display partners to identify a system that expresses MHETase at high density on

109   the cell surface, and demonstrated that the resulting whole-cell catalyst hydrolyses a MHET

110   analog without the need for purification of the MHETase enzyme. The activity of the MHETase

111   whole-cell catalyst is similar to purified recombinant MHETase and is stable to alkaline pH,

112   temperature, and for at least 12 days, a clear advantage over the purified enzyme. We anticipate

113   that large-scale fermentation of the MHETase whole-cell biocatalyst will provide a low-cost

114   source of MHETase suitable for PET plastic recycling, up-cycling, and remediation.

115

Results and Discussion

MHETase cell surface display modules

Our goal was to develop a system expressing the MHETase enzyme, from *I. sakaiensis*, in *S. cerevisiae* to process the product of PET-hydrolysis intermediate MHET (Figure 1A). Surface display is an ideal context for reactions with large substrates, like PET, that cannot translocate to the cell interior [32]. Additionally, surface display circumvents enzyme purification as a prerequisite for catalysis, avoids product contamination [33], facilitates reuse of the catalyst, and can increase catalyst stability [25,34]. We engineered a MHETase cell surface display system to probe these potential advantages relative to conventional enzyme expression and purification. The MHETase surface display system consists of an engineered transcription unit stably integrated at the *CAN1* locus driven by a doxycycline-inducible promoter (WTC846pr) to express MHETase fusion proteins (Figure 1B) [35]. The MHETase fusion contains *(i)* a secretion signal (from the *OST1* gene) fused to the N-terminus of the MHETase coding sequence, *(ii)* a yeast codon-optimized sequence of MHETase from *I. sakaiensis* followed by *(iii)* the coding sequence of GFP and *(iv)* the coding sequence of one of 6 display partners, namely *AGA2*, *CCW12*, *CIS3*, *CWP2*, *SED1* and *TIP1*, which encode yeast cell wall proteins, to allow anchoring of the MHETase protein chimera on the yeast surface (Figure 1B) [36]. The cell wall proteins used for anchoring at the cell surface were chosen to span different modes of covalent linkage to the cell wall, different molecular weights, and different expression levels (Figure 1B). We also designed modules driving secretion of soluble MHETase or intracellular MHETase, as controls.

6

139   *Efficient expression of MHETase display chimeras in vivo*

140   Having successfully assembled the 8 MHETase modules, we measured protein

141   expression using the GFP present in each chimeric protein. To accurately convert GFP

142   fluorescence *in vivo* to protein abundance, we assembled a calibrating set of strains expressing

143   GFP-tagged proteins with abundance ranging from 2.3×10^3 to 7.5×10^5 molecules/cell (Figure

144   2A) [37]. The correlation between protein abundance and normalized GFP intensity was

145   excellent ($R^2 = 0.874$, Figure 2A). Using the normalized GFP intensity measurements for the

146   MHETase chimeras after 4 hours of induction, we calculated MHETase abundance in

147   molecules/cell using the calibration curve (Figure 2B). MHETase chimeras were expressed at

148   similar levels, ranging from 9.3×10^4 (MHETase-Tip1) to 1.5×10^5 (MHETase-Cis3)

149   molecules/cell, corresponding to MHETase concentrations of 16 to 25 nM for cultures

150   containing 10^8 cells/mL (Figure 2B). The intracellular and the secreted MHETase were

151   expressed at slightly higher levels (30 and 27 nM, respectively) compared to the MHETase

152   display chimeras. When we assessed the expression level of the chimeras lacking MHETase, it

153   became apparent that the MHETase sequences reduced protein expression, except for the Ccw12

154   fusion (Figure 2B). It is possible that the display partners, except Ccw12, do not tolerate

155   additional cargo without some reduction of expression. Alternatively, there could be toxicity

156   associated with MHETase expression. We compared growth of the strains expressing MHETase

157   display chimeras with the growth of strains expressing GFP display chimeras. Only MHETase-

158   Aga2 and MHETase-Cis3 resulted in a statistically-supported decrease in growth rate (Figure

159   2C), and the effect size was very small (approximately 5% decrease in growth rate). We

160   conclude that MHETase expression is not toxic to the yeast platform.

161

7

162   *An image analysis pipeline to quantify surface-displayed proteins*

163   Total MHETase abundance does not accurately reflect the enzyme concentration at the

164   cell surface. Secreted proteins can be retained intracellularly, reducing the amount of catalyst

165   that is able to contact substrate outside of the cell, although display of cargos often has efficiency

166   above 50% [38]. We developed a computational pipeline to analyse fluorescence microscopic

167   images of yeast cells expressing surface display proteins to quantify the amount of protein at the

168   cell surface relative to total protein expression. We imaged cells labelled with concanavalin A

169   conjugated to Alexa Fluor 594 (conA-A594) which binds to glycoproteins in the cell wall. Cells

170   were identified based on the conA-A594 fluorescence signal and concentric rings of 1 pixel

171   width inside and outside the conA-A594-defined cell borders were segmented (Figure 3A).

172   Fluorescence intensity was measured for each of the concentric rings. As shown in Figure 3B,

173   the conA-A594 fluorescence signal followed a normal distribution between 0 and -9 pixels and

174   peaked at -4 pixels, consistent with most of the signal being at the periphery of the cell and

175   demonstrating that most of the cell wall signal is between 0 and -9 pixels inside the segmented

176   cell object (Figure 3B). We repeated the analysis with conA-A594 labelled cells expressing

177   Mrh1-GFP, a plasma membrane protein displaying a homogenous fluorescence signal at the cell

178   periphery, as well as the MHETase intracellular chimera, and two additional intracellular GFP-

179   tagged proteins, Tif2 and Rrp1A (Figure 3D). Tif2 and Rrp1A are expressed at 9.2×10^4 and 1.4

180    $\times 10^5$ molecules/cell, respectively, similar to the expression levels of the MHETase display

181   chimeras. As shown in Figure 3B, the fluorescence intensity profile for Mrh1-GFP closely

182   followed that of conA-A594 consistent with Mrh1 residing at the cell periphery. Interestingly,

183   the GFP signal for Mrh1-GFP peaked at the -5 pixels coordinate, while the conA-A595 signal

184   peaked at the -4 pixels coordinate, indicating that our method can distinguish proteins at the

185   plasma membrane from those at the cell wall. The Mrh1 C-terminus (including the GFP tag) is

186   predicted to reside on the inner side of the plasma membrane (Figure S1) consistent with the

187   GFP signal being more internal to the cell compared to the conA-A594 signal. By contrast, the

188   fluorescence profile for the intracellular GFP-proteins did not resemble that of conA-A594 or

189   Mrh1-GFP (Figure 3B). Instead, the fluorescence progressively increased from the -3 pixels ring

190   and plateaued at -6 pixels, demonstrating that most of the signal is more internal as compared to

191   the peak of fluorescence of both the plasma membrane and cell surface (Figure 3B). Even though

192   the fluorescent signal was consistent with intracellular proteins, a significant amount of

193   fluorescence signal was still present within the 0 to -9 ring, indicating bleed-through of

194   intracellular fluorescence into the cell wall ring. For example, approximately 90% and 50% of

195   the intracellular fluorescence intensity is still detected at the -4 and -5 rings, respectively, for all

196   intracellular proteins (Figure 3C). Because the peak of cell surface fluorescence spanned the 0 to

197   -9 pixel rings, we used this entire area to measure displayed abundance and corrected for

198   intracellular fluorescence bleed-through (see Methods).

199

200   *MHETase is displayed efficiently at the cell surface*

201   We determined the fraction of MHETase displayed at the cell surface by measuring the

202   GFP signal at the cell surface relative to total GFP signal by analysis of fluorescence

203   micrographs of cells expressing MHETase chimeras (Figure 3E). GFP intensity was integrated

204   for the 0 to -9 pixel region and corrected for background and intracellular fluorescence bleed-

205   through in the cell wall region and expressed as a ratio to total cell integrated GFP intensity. The

206   analysis was performed on at least 200 individual cells in 6 replicates. As shown in Figure 3F,

207   between 0.16 and 0.22 of the total MHETase was displayed at the cell surface, depending on the

9

208   display partner. Next, using total abundance and displayed fraction data (Figure 2B, 3F), we

209   calculated the displayed MHETase abundance in molecules/cell and in nanomolar concentration

210   of enzyme for a suspension of cells at 10^8 cells/ml. MHETase protein abundance ranged from 1.5

211   × 10^4 (MHETase-Tip1) to 3.0 × 10^4 (MHETase-Aga2) molecules/cell at the cell surface,

212   corresponding to enzyme concentrations of 2.4 to 4.8 nM for 10^8 cell/ml suspensions (Figure

213   3G). The MHETase-Aga2 and MHETase-Sed1 chimeras had the highest displayed fraction. The

214   displayed protein abundance was more variable for MHETase-Aga2, MHETase-Sed1, and

215   MHETase-Cis3 as compared to the other constructs, suggesting that cells might not display these

216   chimeras uniformly. Although the displayed abundance for the MHETase-Aga2 (1.5 × 10^4

217   molecules/cell) was consistent with those described for Aga1-Aga2 yeast surface display systems

218   [32], none of the display partners moved more than 22% of total MHETase to the cell surface.

219   Display efficiencies of over 50% have been described [38], and so we infer that there remains

220   substantial room to improve the efficiency of our MHETase yeast surface display systems.

221

222   *Kinetic analysis of MHETase whole-cell catalysts*

223   Having established that the MHETase constructs were expressed and displayed on the

224   cell surface, we tested whether the MHETase whole-cell biocatalyst had the expected catalytic

225   activity. MHETase activity is readily assayed with the colorimetric substrate MpNPT, and

226   MHETase hydrolysis of MpNPT accurately reflects hydrolysis of MHET [29]. After 4 hours of

227   induction, cells expressing MHETase chimeras were incubated with increasing concentrations of

228   MpNPT and pNP formation was quantified. Enzymatic activity was normalized to 10^8 cell/ml so

229   that the different surface display chimeras could be compared. As shown in Figure 4A-F, all

230   MHETase chimeras followed Michaelis-Menten kinetics. Differences in reaction rates and in

10

231   substrate affinity were readily observable between chimeras, with MHETase-Aga2 performing

232   poorly and MHETase-Tip1 having the highest reaction rate (Figure 4A-F). Importantly, cells

233   expressing intracellular MHETase did not hydrolyse MpNPT, demonstrating that MpNPT is

234   hydrolysed by the surface-displayed MHETase (Figure 4G). Recombinant MHETase produced

235   in *E. coli* or secreted by yeast behaved similarly to the displayed MHETase chimeras (Figure 4H-

236   I). Assays of 7 independent isolates of the MHETase-Tip1 chimera showed a high degree of

237   reproducibility (Figure 4J), indicating that the whole-cell catalyst system is stable and robust to

238   variation.

239   To accurately compare the different MHETase chimeras to purified MHETase, kinetic

240   parameters were calculated using the Michaelis-Menten plots, the enzyme concentration

241   determined from total abundance, the display efficiency, and the cell culture density (Table 1).

242   Again, differences between MHETase chimeras were readily observable. We found that the

243   turnover number (k_{cat}) for whole-cell catalysts were similar to MHETase purified from *E. coli* or

244   MHETase secreted from yeast cells. MHETase-Tip1 k_{cat} was 68% of purified MHETase and

245   96% of secreted MHETase (Table 1). K_m values for the displayed chimeras were 3.6- to 15.7-

246   fold greater than recombinant or secreted MHETase, indicating that surface display reduced the

247   substrate affinity of MHETase. Consequently, catalytic efficiency for the whole-cell MHETase

248   catalysts was also lower compared to recombinant or secreted MHETase. Lower substrate

249   affinity and catalytic efficiency could be due to ectopic glycosylations that are typical of proteins

250   transiting through the yeast secretory pathway [39]. However, the K_m of MHETase secreted from

251   yeast was indistinguishable from that of purified MHETase, suggesting that glycosylation is not

252   causing lower substrate affinity. We suggest that the reduced K_m of the surface displayed

253   chimeras could reflect the environment of the yeast cell surface. As such, mutations that alter cell

11

254   surface properties would be reasonable targets for improving the MHETase display platform.

255   Interestingly, no correlation was evident between the activity of the different chimeras and

256   expression at the cell surface, suggesting that the identity and the mode of cell surface anchoring

257   itself might be responsible for the catalytic efficiency differences that we observe. Nevertheless,

258   the displayed MHETase chimeras differ only modestly from purified MHETase, and our

259   analyses highlight the importance of testing multiple surface display partners to identify

260   chimeras with optimal catalytic properties.

261

262   *The MHETase whole-cell catalyst is stable to alkaline pH, temperature and, time*

263   We next established optimal reaction parameters for temperature and pH for the whole-

264   cell catalyst. As shown in Figure 5A, enzymatic activity was optimal for all the chimeras at pH

265   7.5. At higher pH (pH 9.5 and 10.5), the system remained active, but activity was reduced by

266   approximately 40 to 50%, which contrasts with purified MHETase which remained active at

267   higher pH [29]. The differences observed for activity at pH 7.5 between the different chimeras

268   (Figure 4) remained consistent across the pH range, with MHETase-Tip1 being the most active

269   and MHETase-Aga2 displaying the lowest activity. Similarly, we assessed the effect of

270   temperature on enzyme activity. As shown in Figure 6B, activity steadily increased and peaked

271   at 45°C for all the chimeras. At 55°C, MHETase activity was lower. Therefore, of the tested

272   temperatures, 45°C was optimal, with MHETase activity approximately 3-fold higher than at

273   24°C. Again, differences between chimeras were consistent across temperatures. Purified

274   recombinant MHETase also showed optimal activity at 45°C, in agreement with previous

275   characterizations of purified MHETase [29].

276   Surface display systems for PETase show little loss of enzyme activity over 7 days

277   [25,40], whereas soluble PETase loses activity more rapidly. We compared the activity of

278   surface displayed MHETase to soluble purified MHETase after 12 days at room temperature in

279   phosphate buffer. Surprisingly, we observed that activity increased over time including for the

280   cells expressing intracellular MHETase (Figure 5D, compare day 0 with day 4 or day 12).

281   Interestingly, we noticed that cell count decreased over the same period of time by an average of

282   2- and 6.7-fold at day 4 and day 12, respectively, suggesting that cell lysis was occurring and that

283   release of intracellular MHETase could be the mechanism by which activity is increasing. To test

284   this hypothesis, we repeated enzymatic assay on precipitated cells washed with fresh phosphate

285   buffer and on the supernatant of unwashed cells (Figure 5D). We observed strong activity in the

286   supernatant, representing approximately 70-80% of enzymatic activity of the unwashed cell

287   suspensions. We suggest that some caution is warranted in interpreting display stability results

288   unless the whole-cell catalyst is washed prior to assay. Despite the finding that most of the

289   MHETase activity at 12 days is no longer associated with the yeast cells, MHETase activity of

290   the Aga2, Cis3, and Sed1 chimeras at the cell surface remained stable for 12 days (Figure 6D).

291   By contrast, soluble purified MHETase was inactive after 4 days at room temperature

292   demonstrating that the whole-cell catalyst is considerably more stable to prolonged incubation

293   than the purified enzyme (Figure 6E).

294

295   **Conclusions**

296   We have established a new system for degrading MHET, an important by-product of PET

297   plastic degradation. Using a yeast surface display strategy and testing multiple display fusion

298   partners, we demonstrate the production of MHETase at nanomolar concentrations in cell

13

299   suspensions of moderate density (10^8 cells/ml). We found that Aga2 was a poor display partner

300   for MHETase. Although we note that display efficiency of MHETase-Aga2 was good, the K_m of

301   MHETase-Aga2 was 4.4-fold higher than that of MHETase-Cwp2, and 16-fold higher than

302   purified MHETase. We present alternative display partners for MHETase, including Tip1, Cwp2,

303   and Sed1, that have suitable kinetic and display properties. MHETase whole-cell catalysts were

304   stable for at least 12 days and retained activity up to 45°C. Stability gains relative to purified

305   soluble MHETase when combined with time and cost savings realized by avoiding enzyme

306   purification indicate that yeast surface display is a viable route for MHETase production. Finally,

307   the yeast platform is amenable to synthetic biology, -omics, genetic, and artificial evolution

308   strategies to improve the characteristics of the MHETase whole-cell catalyst.

309

310

311 **Methods**

312 *Yeast maintenance and growth conditions*

313   Yeast strains were maintained at 30°C in standard rich (YPD; 20 g/L peptone, 20g/L

314 dextrose, 10 g/L yeast extract) or synthetic medium containing all amino acids (SDall; 6.7 g/L

315 yeast nitrogen base, 20 g/L glucose). For MHETase induction, yeast strains were grown to

316 saturation overnight in YPD and diluted 6-fold in fresh YPD containing doxycycline at a final

317 concentration of 10 μg/mL. Cells were then grown for 4 hours with agitation at 30°C. Typical

318 cell concentrations after 4 hours of induction were $\sim 10^8$ cell/mL. For MHETase secretion, the

319 same induction scheme was used but cells were pre-grown in fully-supplemented synthetic

320 medium (SDall) and induced in SDall containing 10 μg/ml doxycycline.

321

322 *Yeast strain construction*

323   Yeast transformation was performed using the standard lithium acetate procedure. For

324 CRISPR/Cas9 transformations, yeast cells were transformed using the pUB1306 plasmid (A kind

325 gift of Elçin Ünal, originally generated by Gavin Schlissel and Jasper Rine) containing one of the

326 following guide RNAs (CAN1 gRNA: GATACGTTCTCTATGGAGGA; OST1-GFP gRNA:

327 TCATCGGCAATGGTCAGTAA) and transformants were selected on synthetic medium lacking

328 uracil. URA+ transformants were then on 5-FOA medium to select against cells carrying the

329 CRISPR/Cas9 plasmid. Transformants were validated by PCR and GFP expression was

330 confirmed microscopically.

331   All strains were constructed in DHY213 (a derivative of BY4741 with higher sporulation

332 efficiency and improved mitochondrial function [41]) and are listed in Table S1. To allow

333 doxycycline induction of the WTC846 promoter [35], DHY213 was first modified by integrating

15

334 the linearized FRP2370 plasmid (Addgene #127576), which encodes a cassette expressing the

335 Tet repressor, yielding strain RLKY218 (Table S1). All subsequent strains were constructed in

336 the RLKY218 background via CRISPR/Cas9 mediated assembly of PCR fragments at the *CAN1*

337 locus. A first set of strains with the following construct architecture was generated: *WTC846pr-*

338 *OST1ss-GFP-display_partner-PRM9ter*. WTC846pr is a strong doxycycline inducible promoter,

339 *OST1ss* is the Ost1 endoplasmic reticulum translocation signal to allow for efficient secretion

340 [36], GFP is the yeast codon-optimized monomeric GFP [42,43], *display_partner* is the coding

341 sequence of one of *SED1*, *AGA2*, *CCW12*, *CWP2*, *CIS3* or *TIP1* lacking their respective

342 secretion signals, and *PRM9ter* is the terminator region of *PRM9* (Table S2). The display partner

343 sequences were codon optimized to minimize chances of recombination between the endogenous

344 loci and the synthetic constructs, which were integrated at *CAN1*. Codon optimization was

345 performed using the "Optimize codon" function of Benchling (https://www.benchling.com/)

346 using *Saccharomyces cerevisiae* as "Organism". This first set of strains was then used as

347 platform for integration of the yeast codon optimized MHETase gene from *I. sakaiensis* (devoid

348 of its endogenous secretion signal) between the *OST1ss* and the *msGFP* sequence (Table S2). All

349 DNA sequences described here are provided in the Table S2.

350

351 *Measuring MHETase total protein abundance*

352 Expression was induced as described above. After 4h of induction, cells were washed

353 twice with sterile water and resuspended in the same volume of sterile water. 200 μL of cells

354 were transferred into a clear 96-well plate and GFP fluorescence intensity was measured. The

355 same cell suspension was diluted 10 times and used to measure optical density at 600nm (OD_{600}).

356 All measurements were made using a CLARIOstar (BMG LABTECH) plate reader. For each

357 strain, GFP intensity was first corrected for cell mass by dividing GFP intensity by OD_{600}

358 (GFP_{corr}). GFP_{corr} values were then expressed as a ratio (GFP_{norm}) between GFP_{corr} for a given

359 GFP expressing strain and GFP_{corr} obtained for a GFP negative control strain (DHY213).

360 To establish a GFP standard curve, the following strains were obtained from the GFP

361 strain collection [37,44]: *PEX21-GFP, FMP23-GFP, MDL2-GFP, PER1-GFP, LPX1-GFP,*

362 *YML007CA-GFP, RAI1-GFP, SPI1-GFP, RTG2-GFP, MOT2-GFP, RRP15-GFP, RET2-GFP,*

363 *GCN20-GFP, RPC40-GFP, NEW1-GFP, ARB1-GFP, OLA1-GFP, RPL2A-GFP, PMP2-GFP,*

364 *STM1-GFP, TIF2-GFP, HTB2-GFP, RPS1B-GFP, RPP1A-GFP, SSA2-GFP, SSA1-GFP, TEF2-*

365 *GFP, TEF1-GFP, PDC1-GFP, TDH3-GFP* and their GFP fluorescence intensity was measured.

366 Regression analysis was performed with GFP_{norm} values for the GFP strains and the median

367 molecules/cell data from Ho *et al* [37,44], using GraphPad Prism 5. GFP_{norm} values obtained for

368 the various surface display constructs were then used to calculate their respective abundances

369 using the regression equation determined from the GFP standard curve.

370

371 *Measuring MHETase cell surface abundance*

372 Cells were induced in YPD as described above. After 4 hours of induction cells were

373 washed in sterile water twice and resuspended in water containing 10 μm/mL concanavalin A

374 conjugated with Alexa Fluor 594 (Thermo Fisher Scientific) and incubated at room temperature

375 for 1 hour. GFP and Alexa Fluor 594 imaging was performed on an Opera Phenix (Perkin Elmer)

376 high-throughput confocal microscope at a focal height of 1.5 μm using 488 nm and 561 nm

377 excitation lasers and 500-550 nm, 570-630 nm bandpass emission filters. Images were analyzed

378 with CellProfiler 3.1.9 (https://cellprofiler.org/) using the custom pipeline provided in the

379 supplementary material.

17

380   To determine the position of cell surface with respect to the outline of the segmented cell

381   objects, cells were first identified and segmented using Alexa Fluor 594 fluorescence images.

382   Cell objects were further segmented into 10 inward and 4 outward concentric rings of one pixel

383   width except for the most inward ring which represented the remaining inner portion of the cell.

384   Median fluorescence was determined in each ring and corrected for background fluorescence

385   before being normalized by the signal of most inner portion of the cell. Cell wall signal was

386   determined as the area of strongest concanavalin A signal, which spanned a ring of 9 pixels

387   width inside the cell object (Figure 3B, conA-A594 curve). This analysis was also performed on

388   cells expressing known intracellular GFP-tagged proteins (Rrp1a-GFP, Tif2-GFP and intra-M

389   chimera) to determine the average fraction of inner fluorescence signal spreading into each of the

390   cell wall rings defined above (Figure 3B). The fraction of inner fluorescence was termed FB_i

391   (Fluorescence Bleed, where i represents a given 1-pixel width ring). This parameter was used in

392   the analysis below.

393   To determine the abundance of MHETase at the cell surface, the GFP intensity was

394   integrated for the entire cell object and for the 9 inner rings closest to the cell object outer edge

395   and expressed as a ratio of integrated GFP in the cell wall ring over the integrated GFP for the

396   entire cell. We refer to this ratio as the fraction of GFP displayed or display efficiency. To

397   account for background fluorescence and intracellular bleed-through fluorescence, two

398   normalizations were applied before calculating the fraction of GFP displayed. First, all raw

399   integrated GFP values were corrected for background fluorescence as follows: $GFPint_{corr1} =$

400     $GFPinti - (GFPmed_{backd} \times P_i)$, where $GFPint_i$ is the raw GFP integrated value for a given

401   ring or the total cell, $GFPmed_{backd}$ is the median background fluorescence determined from an

402   area of the image with no cells and P_i the number of pixels in the area considered (ring or total

18

403   cell). Second, bleed-through fluorescence was also taken into account for integrated GFP values

404   of each of the 9 cell wall rings, as follows: $GFPint_{corr2} = GFPint_{corr1} - (GFPmed_{inner} \times$

405    $FB_i \times P_i)$, where $GFPmed_{inner}$ is the background corrected median GFP fluorescence intensity

406   for the inner part of the cell, FB_i is the fluorescence bleed-through correction factor for the area

407   considered, as determined above, and P_i the number of pixels in the ring area considered.

408   Displayed ratio was then calculated as the sum of $GFPint_{corr2}$ values from the cell wall rings and

409   divided by $GFPint_{corr1}$ obtained for the total cell. At least 200 cells were analyzed in each

410   technical (n=2) and biological replicates (n=3).

411

412   *Measurement of strain fitness*

413   Fitness was measured as previously described [45]. Briefly, cells were grown to

414   saturation overnight and diluted 100-fold in 200 μL of fresh YPD with or without doxycycline

415   (10 μg/mL) in a transparent 96-well plate. OD600 was monitored every 15 minutes in a Genios

416   Tecan plate reader. Growth rate was determined in R (https://www.r-project.org/). Fitness was

417   calculated as the ratio of the growth rate of the experimental strain to that of the parental strain

418   (DHY213).

419

420   *MHETase activity measurement with the whole-cell biocatalyst*

421   Induced cells were washed twice in sterile water and resuspended in same volume with

422   111 mM phosphate buffer at pH 7.5, 8.5, 9.5 or 10.5. Cell concentration was determined using a

423   Beckman-Coulter Counter Z1 equipped with a 100 μm aperture tube using a particle lower

424   threshold limit of 4 μm. 270 μL of cells were mixed with 30 μL of MpNPT (CAS #1137-99-1,

425   Toronto Research Chemicals) at ten times the final concentration in DMSO, and reaction was

19

426   allowed to proceed for 10 minutes. The reaction was stopped by separating the cells from the

427   reaction with a 96-well filter plate (AcroPrep, Pall) mounted on a vacuum device (NucleoVac 96,

428   Macherey-Nagel). Alternatively, miniprep columns were used for filtering (PuroSPIN MINI,

429   Luna Nanotech). 120 µL of filtered reaction was then transferred into a clear 384-well plate, to

430   increase the light pathlength, and *para*-nitrophenol (pNP) concentration was determined by

431   measuring absorbance at 405nm in a CLARIOstar plate reader (BMG LABTECH). Each run

432   included an MpNPT autohydrolysis control (MpNPT diluted in phosphate buffer only). The

433   molar extinction coefficients at 407nm for pNP at the different pH's were calculated from Biggs

434   (1954) [46] and are provided in Figure S2. All reactions were performed at 24°C unless specified

435   otherwise. To assess activity at different temperatures, cells were pre-incubated in a water bath at

436   the given temperature for 10 minutes before addition of the substrate and held at the same

437   temperature after addition of MpNPT. To test the stability of the whole-cell biocatalyst, induced

438   cells were resuspended in phosphate buffer pH 7.5 and held for 12 days at room temperature

439   without agitation.

440

441   *Purification, quantification, and activity measurement of recombinant MHETase from E. coli*

442   Recombinant MHETase was purified as described previously [29] with some

443   modifications. *E. coli* Shuffle T7 express cells were transformed with pCOLDII-MHETase

444   vector [29] and selected on agar plates containing 100 µg/mL carbenicillin at 30°C. Single

445   colonies were inoculated into liquid growth medium containing carbenicillin and protein

446   expression was induced as follows. 1L cultures were grown to an OD of ~0.5 at 30°C, then

447   rapidly cooled in an ice bath to ~10°C. Isopropyl β-D-1-thiogalactopyranoside (IPTG) was

448   added to a final concentration of 1 mM, and cultures were incubated overnight at 16°C with

20

449   shaking. Cell pellets were collected by centrifugation at 16,770 g at 4°C, resuspended in 50mM

450   Tris-HCl (pH 7.5), 100 mM NaCl, 10 mM imidazole, 1 mM DTT, and protease inhibitors (2

451   μg/mL aprotonin, 10 μM bestatin, 10 μM leupeptin, 1 μM pepstatin, and 0.5 mM PMSF), and

452   lysed by sonication then clarified by ultracentrifugation (4°C, 142,000 g, 1 hour). The clarified

453   lysates were loaded onto a 5 mL His-Trap FF column (Cytiva), washed with 50 mM Tris-HCl

454   (pH 7.5), 100 mM NaCl, 20 mM imidazole and 1 mM DTT, and then eluted in 50 mM Tris-HCl

455   (pH 7.5), 100 mM NaCl and 500 mM imidazole. Peak fractions were pooled and diluted with 25

456   mM Tris-HCl (pH 7.5) to a final concentration of ~50 mM NaCl before loading onto a 5 mL

457   HiTrap Q HP column (Cytiva) pre-equilibrated in 25 mM Tris-HCl (pH 7.5) and 50 mM NaCl.

458   The column was then washed using 10 column volumes of 25 mM Tris-HCl (pH 7.5) and 50 mM

459   NaCl, followed by a 0.05-1 M NaCl salt gradient over 10 column volumes. As most of the

460   recombinant MHETase eluted in the wash, the wash fraction was concentrated to a final volume

461   of ~500 μL with an Ultra-15 10kDa MWCO centrifugal concentrator (Amicon) and then loaded

462   onto a Superdex 75 Increase 10/300 GL column (Cytiva). Recombinant MHETase was then

463   eluted in 20 mM Tris-HCl (pH 7.5) and 150 mM NaCl at 0.5 mL/min and peak fractions were

464   pooled. Protein purity was assessed by SDS-PAGE (Figure S3) and protein concentration was

465   measured spectrophotometrically using $\varepsilon_{280} = 102{,}330$ M^{-1}cm^{-1}. Protein aliquots were snap-frozen

466   prior to being stored at -80°C.

467   Recombinant MHETase activity was measured as described previously [29] in 100 mM

468   sodium phosphate buffer (pH 7.5) at 24°C. Enzymatic parameters were similar to published data

469   for MHETase using MpNPT as substrate [9,29]. To assess activity at different temperatures,

470   MHETase in 100 mM phosphate buffer pH 7.5 was pre-incubated in a water bath at the given

471   temperature for 20 minutes before addition of the substrate and held at the same temperature

21

472   after addition of MpNPT. The enzyme was freshly thawed before each assay. To determine

473   stability over time, the recombinant enzyme was kept at room temperature in 100 mM sodium

474   phosphate buffer (pH 7.5) for 4 days without shaking.

475

476   *Purification, quantification, and activity measurement of MHETase secreted from yeast*

477   Cultures of RLKY245 (intracellular MHETase control) and RLKY247 (*OST1-MHETase-*

478   *GFP*) were grown overnight in SDall at 30°C. The overnight culture was then induced by the

479   addition of 10 µg/ml doxycycline as described above. After 4 hours of induction, cells were

480   centrifuged at 3500 rpm for 5 minutes at room temperature, and the supernatant was collected

481   and kept on ice throughout the remainder of the procedure. The supernatant was concentrated to

482   a final volume of ~300 µL, and buffer exchanged to 100 mM sodium phosphate buffer pH 7.5

483   (Amicon Ultra-4, Millipore Sigma). The concentrated sample was stored at 4°C for a maximum

484   of one week.

485   MHETase concentration was measured by ELISA. Samples were diluted 2-, 4- and 8-fold

486   in sodium phosphate pH 7.5. Clear flat-bottom Immuno Nonsterile 96-well plates (Thermo

487   Fisher Scientific) were coated with the samples, or with serial dilutions of purified GFP

488   (Invitrogen; concentration range of 0.1-50 ng/mL) at 4°C overnight. The coating solution was

489   then removed and 200 µL of blocking buffer (1x PBS, 3% non-fat milk, 0.1% Tween-20) was

490   added to each well and incubated at room temperature for 1 hour. After removal of the blocking

491   solution 100 µL of anti-GFP (Living Colors GFP monoclonal antibody, Clontech) diluted

492   1:10,000 in antibody solution (1x PBS, 1% non-fat milk, 0.1% Tween-20) was added to each

493   well and incubated at room temperature for 2 hours. Plates were washed 3 times for 5 minutes

494   each with PBS-T (1x PBS, 0.1% Tween 20). After removing the wash solution, 50 µL of anti-

495   mouse-HRP (Pierce) diluted 1:10,000 in antibody solution was added to the plates, and incubated

496   for 1 hour at room temperature. Plates were then washed 3 times for 5 minutes each with PBS-T

497   at room temperature. After removing the wash solution, 100 μL of TMB substrate (Thermo

498   Fisher Scientific) was added to each well. The reaction was incubated in the dark at room

499   temperature for a maximum of 10 minutes and stopped by adding 50 μL of 2 N HCl to each well.

500   Absorbance was measured at 450nm on a microplate reader (CLARIOstar, BMG LabTech) and

501   measurements from RLKY245 supernatant were used as the negative control for the

502   measurements of the RLKY247 supernatant. MHETase activity was assayed as described above

503   for the recombinant MHETase purified from $E. coli$.

504

511

512   **Author contributions**

513   Conceptualization, RLK, VS, and GWB; Methodology, RLK, VS, MWF, BH, BJP, and

514   GWB; Protein purification, MWF and BJP; Experimentation, RLK, MWF, and BH; Strain

515   engineering, VS, JB and SP; Formal Analysis, RLK, MWF, BH, and GWB; Funding acquisition,

516   HDMW and GWB; Writing, RLK, MWF, BH, and GWB; Review & Editing, RLK, VS, MWF,

517   BH, BJP, JB, SP, HDMW, and GWB.

518

Funding

520   This work was supported by Natural Sciences and Engineering Research Council of

521 Canada grants RGPIN-2017-06855 to GWB and RGPIN-2017-06670 to HDMW. GWB and

522 HDMW hold a Canada Research Chairs. The funding bodies had no role in the design of the

523 study, in collection, analysis, and interpretation of data, or in writing the manuscript.

524

Availability of data and materials

526   All data supporting the conclusions of this study are included within the article and its

527 additional files.

528

Declarations

530 *Ethics approval and consent to participate*

531   Not applicable

532 *Consent for publication*

533   Not applicable

534 *Competing interests*

535   The authors declare that they have no competing interests.

536

537

538

References

1. Soong YHV, Sobkowicz MJ, Xie D. Recent Advances in Biological Recycling of Polyethylene Terephthalate (PET) Plastic Wastes. Bioengineering. 2022;9.

2. Plastics - the Facts 2021. www.plasticseurope.org/knowledge-hub/plastics-the-facts-2021/.

3. Wyeth NC, Al- E, Convers N, Ronald W, Roseveare N. Biaxially oriented poly(ethylene terephthalate) bottle. 1970.

4. Toussaint B, Raffael B, Angers-Loustau A, Gilliland D, Kestens V, Petrillo M, et al. Review of micro- and nanoplastic contamination in the food chain. Food Additives & Contaminants: Part A. 2019;36:639–73.

5. Ragusa A, Svelato A, Santacroce C, Catalano P, Notarstefano V, Carnevali O, et al. Plasticenta: First evidence of microplastics in human placenta. Environ Int. Environ Int. 2021;146.

6. Schwabl P, Koppel S, Konigshofer P, Bucsics T, Trauner M, Reiberger T, et al. Detection of Various Microplastics in Human Stool: A Prospective Case Series. Ann Intern Med. Ann Intern Med. 2019;171:453–7.

7. Sussarellu R, Suquet M, Thomas Y, Lambert C, Fabioux C, Pernet MEJ, et al. Oyster reproduction is affected by exposure to polystyrene microplastics. Proc Natl Acad Sci U S A. 2016;113:2430–5.

8. Lu L, Wan Z, Luo T, Fu Z, Jin Y. Polystyrene microplastics induce gut microbiota dysbiosis and hepatic lipid metabolism disorder in mice. Sci Total Environ. Sci Total Environ. 2018;631–632:449–58.

9. Yoshida S, Hiraga K, Takehana T, Taniguchi I, Yamaji H, Maeda Y, et al. A bacterium that degrades and assimilates poly(ethylene terephthalate). Science. 2016;351:1196–9.

10. Joo S, Cho IJ, Seo H, Son HF, Sagong HY, Shin TJ, et al. Structural insight into molecular mechanism of poly(ethylene terephthalate) degradation. Nat Commun. Nat Commun. 2018;9.

11. Lu H, Diaz DJ, Czarnecki NJ, Zhu C, Kim W, Shroff R, et al. Machine learning-aided engineering of hydrolases for PET depolymerization. Nature. 2022;604:662–7.

12. Tournier V, Topham CM, Gilles A, David B, Folgoas C, Moya-Leclair E, et al. An engineered PET depolymerase to break down and recycle plastic bottles. Nature. 2020;580:216–9.

13. Cui Y, Chen Y, Liu X, Dong S, Tian Y, Qiao Y, et al. Computational Redesign of a PETase for Plastic Biodegradation under Ambient Condition by the GRAPE Strategy. ACS Catal. 2021;11:1340–50.

584   14. Son HF, Cho IJ, Joo S, Seo H, Sagong HY, Choi SY, et al. Rational Protein Engineering of
585   Thermo-Stable PETase from *Ideonella sakaiensis* for Highly Efficient PET Degradation. ACS
586   Catal. 2019;9:3519–26.

588   15. Müller RJ, Schrader H, Profe J, Dresler K, Deckwer WD. Enzymatic degradation of
589   poly(ethylene terephthalate): Rapid hydrolyse using a hydrolase from *T. fusca*. Macromol Rapid
590   Commun. 2005;26:1400–5.

592   16. Sulaiman S, You DJ, Kanaya E, Koga Y, Kanaya S. Crystal structure and thermodynamic
593   and kinetic stability of metagenome-derived LC-cutinase. Biochemistry. 2014;53:1858–69.

595   17. Sulaiman S, Yamato S, Kanaya E, Kim JJ, Koga Y, Takano K, et al. Isolation of a novel
596   cutinase homolog with polyethylene terephthalate-degrading activity from leaf-branch compost
597   by using a metagenomic approach. Appl Environ Microbiol. 2012;78:1556–62.

599   18. Herrero Acero E, Ribitsch D, Steinkellner G, Gruber K, Greimel K, Eiteljoerg I, et al.
600   Enzymatic surface hydrolysis of PET: Effect of structural diversity on kinetic properties of
601   cutinases from *Thermobifida*. Macromolecules. 2011;44:4632–40.

603   19. Sonnendecker C, Oeser J, Richter PK, Hille P, Zhao Z, Fischer C, et al. Low Carbon
604   Footprint Recycling of Post-Consumer PET Plastic with a Metagenomic Polyester Hydrolase.
605   ChemSusChem. 2021.

607   20. Dissanayake L, Jayakody LN. Engineering Microbes to Bio-Upcycle Polyethylene
608   Terephthalate. Front Bioeng Biotechnol. 2021;9.

610   21. Kenny ST, Runic JN, Kaminsky W, Woods T, Babu RP, Keely CM, et al. Up-cycling of PET
611   (polyethylene terephthalate) to the biodegradable plastic PHA (polyhydroxyalkanoate). Environ
612   Sci Technol. 2008;42:7696–701.

614   22. Werner AZ, Clare R, Mand TD, Pardo I, Ramirez KJ, Haugen SJ, et al. Tandem chemical
615   deconstruction and biological upcycling of poly(ethylene terephthalate) to β-ketoadipic acid by
616   *Pseudomonas putida* KT2440. Metab Eng. 2021;67:250–61.

618   23. Sadler JC, Wallace S. Microbial synthesis of vanillin from waste poly(ethylene
619   terephthalate). Green Chemistry. 2021;23:4665–72.

621   24. Kim HT, Kim JK, Cha HG, Kang MJ, Lee HS, Khang TU, et al. Biological Valorization of
622   Poly(ethylene terephthalate) Monomers for Upcycling Waste PET. ACS Sustain Chem Eng.
623   2019;7:19396–406.

625   25. Chen Z, Wang Y, Cheng Y, Wang X, Tong S, Yang H, et al. Efficient biodegradation of
626   highly crystallized polyethylene terephthalate through cell surface display of bacterial PETase.
627   Science of The Total Environment. 2020;709:136138.

628 26. Gamerith C, Vastano M, Ghorbanpour SM, Zitzenbacher S, Ribitsch D, Zumstein MT, et al.
629 Enzymatic degradation of aromatic and aliphatic polyesters by P. pastoris expressed cutinase 1
630 from *Thermobifida cellulosilytica*. Front Microbiol. 2017;8:938.

632 27. da Costa AM, de Oliveira Lopes VR, Vidal L, Nicaud JM, de Castro AM, Coelho MAZ.
633 Poly(ethylene terephthalate) (PET) degradation by Yarrowia lipolytica: Investigations on cell
634 growth, enzyme production and monomers consumption. Process Biochemistry. 2020;95:81–90.

636 28. Kosiorowska KE, Biniarz P, Dobrowolski A, Leluk K, Mirończuk AM. Metabolic
637 engineering of Yarrowia lipolytica for poly(ethylene terephthalate) degradation. Science of The
638 Total Environment. 2022;831:154841.

640 29. Palm GJ, Reisky L, Böttcher D, Müller H, Michels EAP, Walczak MC, et al. Structure of the
641 plastic-degrading *Ideonella sakaiensis* MHETase bound to a substrate. Nat Commun. 2019;10.

643 30. Barth M, Oeser T, Wei R, Then J, Schmidt J, Zimmermann W. Effect of hydrolysis products
644 on the enzymatic degradation of polyethylene terephthalate nanoparticles by a polyester
645 hydrolase from *Thermobifida fusca*. Biochem Eng J. 2015;93:222–8.

647 31. Knott BC, Erickson E, Allen MD, Gado JE, Graham R, Kearns FL, et al. Characterization
648 and engineering of a two-enzyme system for plastics depolymerization. Proc Natl Acad Sci U S
649 A. 2020;117:25476–85.

651 32. Andreu C, del Olmo M. Yeast arming systems: pros and cons of different protein anchors
652 and other elements required for display. Appl Microbiol Biotechnol. 2018;102:2543–61.
653 33. Hartmann M, Kostrov X. Immobilization of enzymes on porous silicas-benefits and
654 challenges. Chem Soc Rev. 2013;42:6277–89.

656 34. Yuzbasheva EY, Yuzbashev T v., Perkovskaya NI, Mostova EB, Vybornaya T v.,
657 Sukhozhenko A v., et al. Cell surface display of *Yarrowia lipolytica* lipase Lip2p using the cell
658 wall protein YlPir1p, its characterization, and application as a whole-cell biocatalyst. Appl
659 Biochem Biotechnol. 2015;175:3888–900.

661 35. Azizoglu A, Brent R, Rudolf F. A precisely adjustable, variation-suppressed eukaryotic
662 transcriptional controller to enable genetic discovery. Barkai N, editor. Elife. 2021;10:e69549.

664 36. Fitzgerald I, Glick BS. Secretion of a foreign protein from budding yeasts is enhanced by
665 cotranslational translocation and by suppression of vacuolar targeting. Microb Cell Fact.
666 2014;13:125.

668 37. Ho B, Baryshnikova A, Brown GW. Unification of Protein Abundance Datasets Yields a
669 Quantitative Saccharomyces cerevisiae Proteome. Cell Syst. 2018;6:192-205.e3.

671 38. van der Vaart JM, te Biesebeke R, Chapman JW, Toschka HY, Klis FM, Verrips CT.
672 Comparison of cell wall proteins of *Saccharomyces cerevisiae* as anchors for cell surface
673 expression of heterologous proteins. Appl Environ Microbiol. 1997;63:615–20.

674   39. Delic M, Valli M, Graf AB, Pfeffer M, Mattanovich D, Gasser B. The secretory pathway:
675   exploring yeast diversity. FEMS Microbiol Rev. 2013;37:872–914.
676
677   40. Jia Y, Samak NA, Hao X, Chen Z, Wen Q, Xing J. Hydrophobic cell surface display system
678   of PETase as a sustainable biocatalyst for PET degradation. Front Microbiol. 2022;13:1005480.
679
680   41. Harvey CJB, Tang M, Schlecht U, Horecka J, Fischer CR, Lin H-C, et al. HEx: A
681   heterologous expression platform for the discovery of fungal natural products. Sci Adv.
682   2018;4:eaar5459.
683
684   42. Kaishima M, Ishii J, Matsuno T, Fukuda N, Kondo A. Expression of varied GFPs in
685   *Saccharomyces cerevisiae*: codon optimization yields stronger than expected expression and
686   fluorescence intensity. 2016;6.
687
688   43. Cinelli RAG, Ferrari A, Pellegrini V, Tyagi M, Giacca M, Beltram F. The Enhanced Green
689   Fluorescent Protein as a Tool for the Analysis of Protein Dynamics and Localization: Local
690   Fluorescence Study at the Single-molecule Level. Photochem Photobiol. 2000;71:771–6.
691
692   44. Huh WK, Falvo JV, Gerke LC, Carroll AS, Howson RW, Weissman JS, et al. Global
693   analysis of protein localization in budding yeast. Nature. 2003;425:686–91.
694
695   45. Loll-Krippleber R, Brown GW. P-body proteins regulate transcriptional rewiring to promote
696   DNA replication stress resistance. Nat Commun. 2017;8.
697
698   46. Biggs AI. A spectrophotometric determination of the dissociation constants of p-nitrophenol
699   and papaverine. Transactions of the Faraday Society. 1954;50:800–2.
700
701

Table 1. Enzymatic parameters for each of the display chimeras, secreted MHETase (secreted-M) and recombinant MHETase purified from *E. coli* (rMHETase).

	rMHETase	M+Aga2	M+Ccw12	M+Cis3	M+Tip1	M+Cwp2	M+Sed1	secreted-M
Vmax (nM/s)[a]	20.51	5.67	16.46	7.03	18.03	13.64	12.19	11.19
Km (μM)[a]	3.11	48.79	12.60	14.58	17.10	11.18	11.62	3.77
total [E] (nM)	1.90	22.78	16.22	24.83	15.50	18.43	17.52	1.47
display efficiency	n.a.	0.10	0.13	0.12	0.13	0.13	0.14	n.a.
displayed [E] (nM)	n.a.	2.35	2.18	3.04	2.07	2.49	2.50	n.a.
kcat (s^{-1})	10.79	2.41	7.55	2.31	8.72	5.49	4.87	7.61
efficiency ($\mu M^{-1}\ s^{-1}$)	3.47	0.05	0.60	0.16	0.51	0.49	0.42	2.02

[a] Vmax and Km were calculated from the Michaelis-Menton curves in Figure 4.
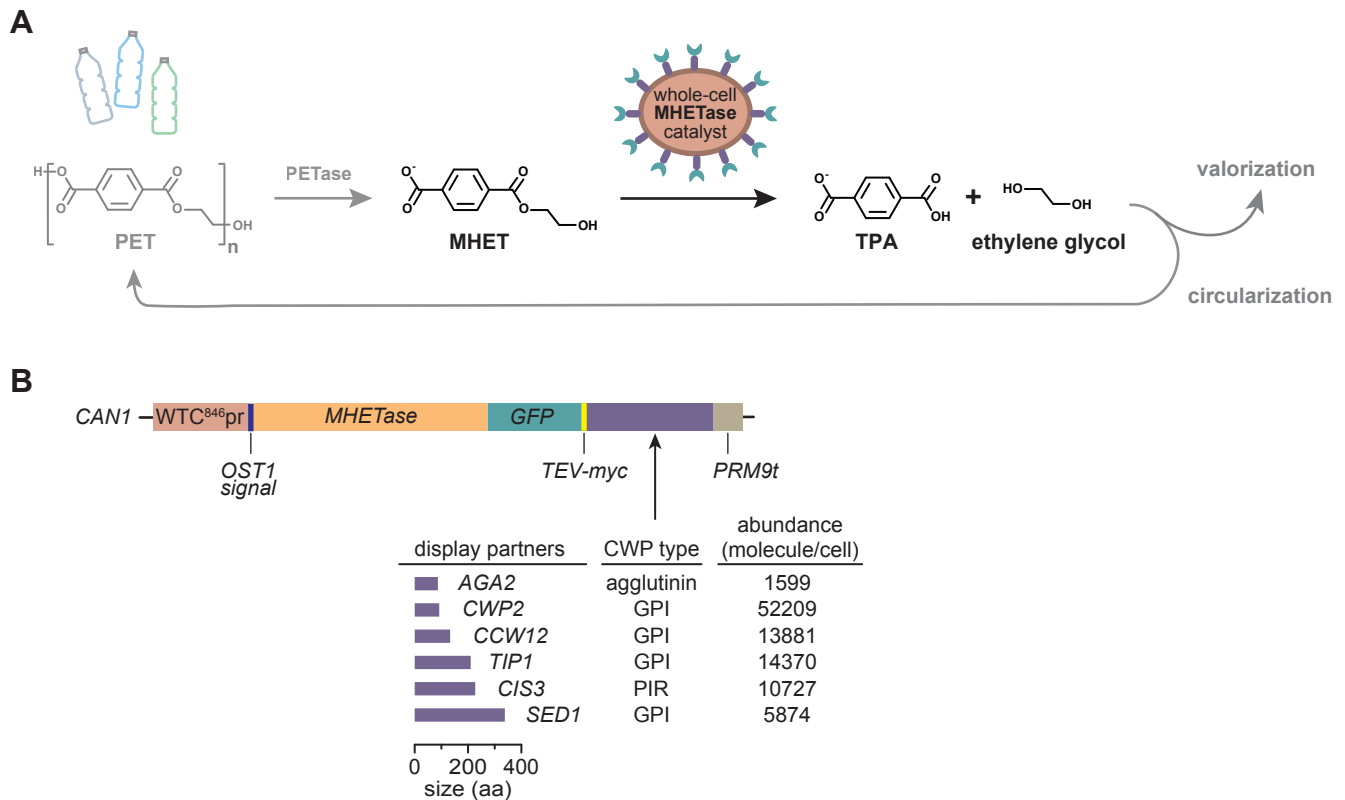
Figure 1. The MHETase whole-cell catalyst concept. A. The MHETase whole-cell catalyst performs the second step of the PET biodegradation pathway. In the first step, repeating units of MHET in the PET polymer are released by the enzyme PETase. MHET is then processed into TPA and ethylene glycol by the MHETase whole-cell catalyst. TPA and ethylene glycol can be used to synthesize new, virgin PET, bio-converted to high-value compounds or simply converted into biomass. **B.** Chimera design for surface display of MHETase. The coloured blocks represent the different components assembled to express MHETase (orange block) at the cell surface. Different cell wall proteins (CWPs; purple block) were fused to MHETase to identify the best design. Amino acid length is indicated, as is CWP type, and expression level for the different CWPs under their native promoters. Control chimeras lacking MHETase were also generated.
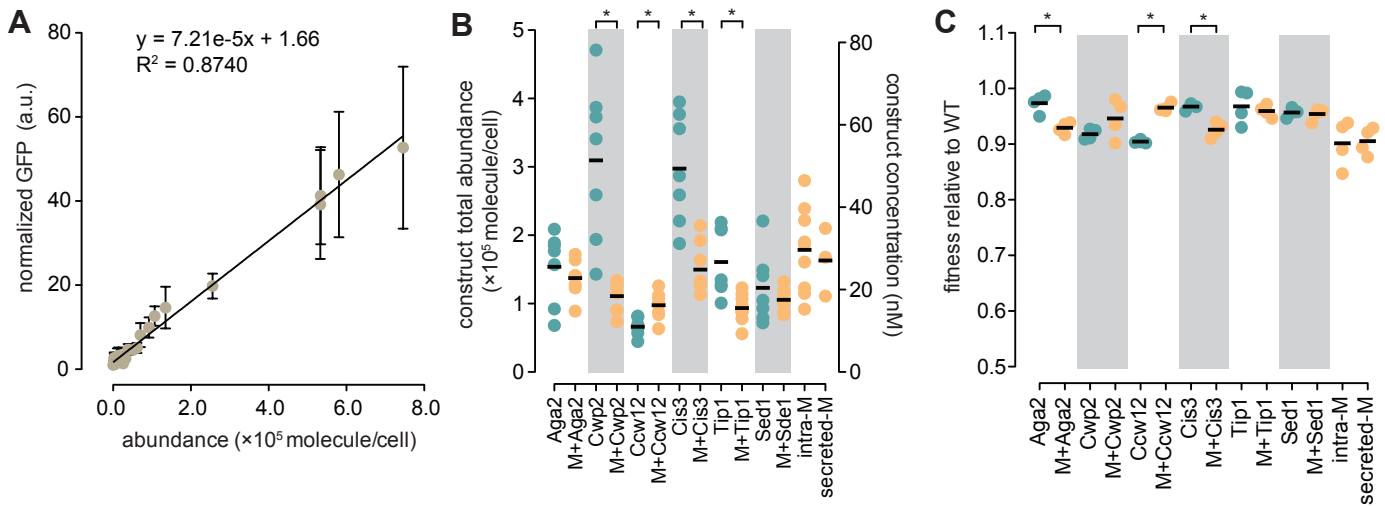
Figure 2. MHETase display constructs are efficiently expressed at minimal fitness cost. A. GFP calibration standards for measuring abundance of MHETase chimeras in molecules per cell. GFP-fusion strains spanning the range of molecules per cells were selected and GFP fluorescence was measured. The regression analysis line and equation are indicated. Bars indicate standard deviation; n ≥ 7. **B.** Abundance of the indicated surface display chimeras with (orange) or without (green) MHETase. Abundance was determined using GFP fluorescence after induction with doxycycline for 4 hours and converted to molecules per cell using the equation in A. Theoretical MHETase molarity was inferred from the molecule/cell data for a cell density of 10^8 cells/ml (right y-axis). Horizontal bars indicate the means of the replicates. Asterisks indicate p-values ≤ 0.05 (unpaired Student's t-test; n = 7). Intracellular MHETase (intra-M) and secreted MHETase (secreted-M) are indicated. **C.** Fitness of cells expressing the surface display chimeras. Cells expressing the indicated chimeras were grown in presence of doxycycline in YPD medium for 24h. Fitness is expressed as a ratio of the growth rate of each strain to that of the wild-type. Horizontal bars indicate the means of the replicates. Asterisks indicate p-values ≤ 0.05 (unpaired Student's t-test; n = 4).
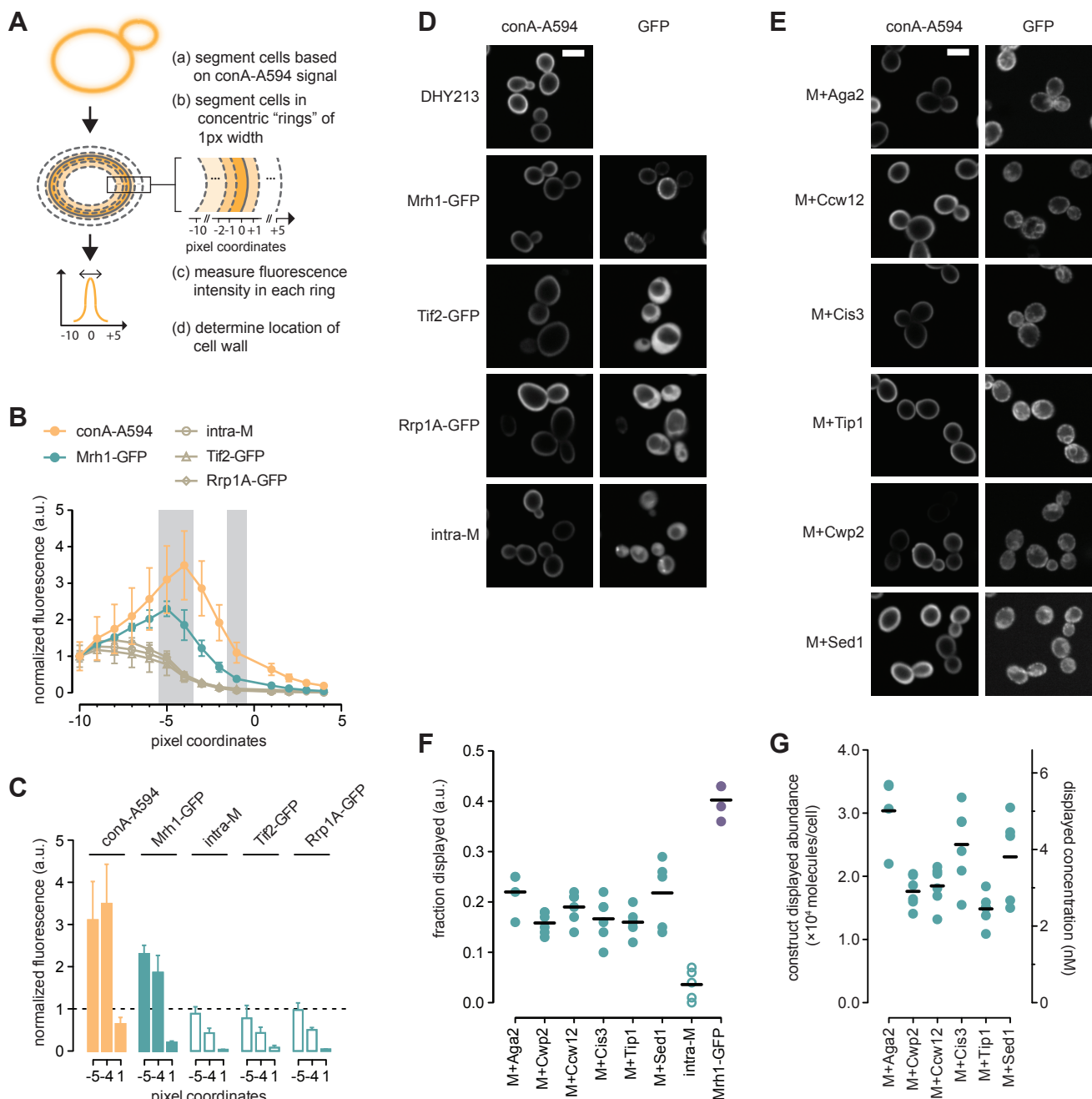
Figure 3. A microscopy-based method to measure MHETase cell surface display efficiency. A. Outline of the microscopy-based method to quantify GFP signal on the cell surface (see text for details). **B.** Mean fluorescence intensities at each pixel coordinate for the indicated strains. Bars indicate standard deviation. Analysis was performed on at least 40 cells in each replicate. conA-A594: n= 98, Mrh1-GFP and intra-cellular MHETase (intra-M): n = 4, Tif2-GFP and Rrp1A-GFP: n = 2. **C.** Comparison of mean fluorescence intensities for the -5, -4, and +1 pixel coordinates for the indicated strains (grey shading in B). Bars indicate standard deviation. **D, E.** Representative fluorescence micrographs for the strains in B and C and for the MHETase surface display chimeras. Scale bar: 5 µm. **F.** Fraction of MHETase chimeras displayed at the cell surface. Cells were induced for 4 hours, labelled with conA-A594 and imaged. The fraction of displayed chimera is plotted. Horizontal bars indicate the means of the replicates (n = 6). Each replicate included at least 200 cells. **G.** Abundance of the MHETase chimeras at the cell surface. The fraction of chimera displayed from panel F was used to calculate the cell surface abundance in molecules per cell. Theoretical construct molarity is indicated for a cell density of 10^8 cells/ml. Horizontal bars indicate the means of the replicates (n = 6).
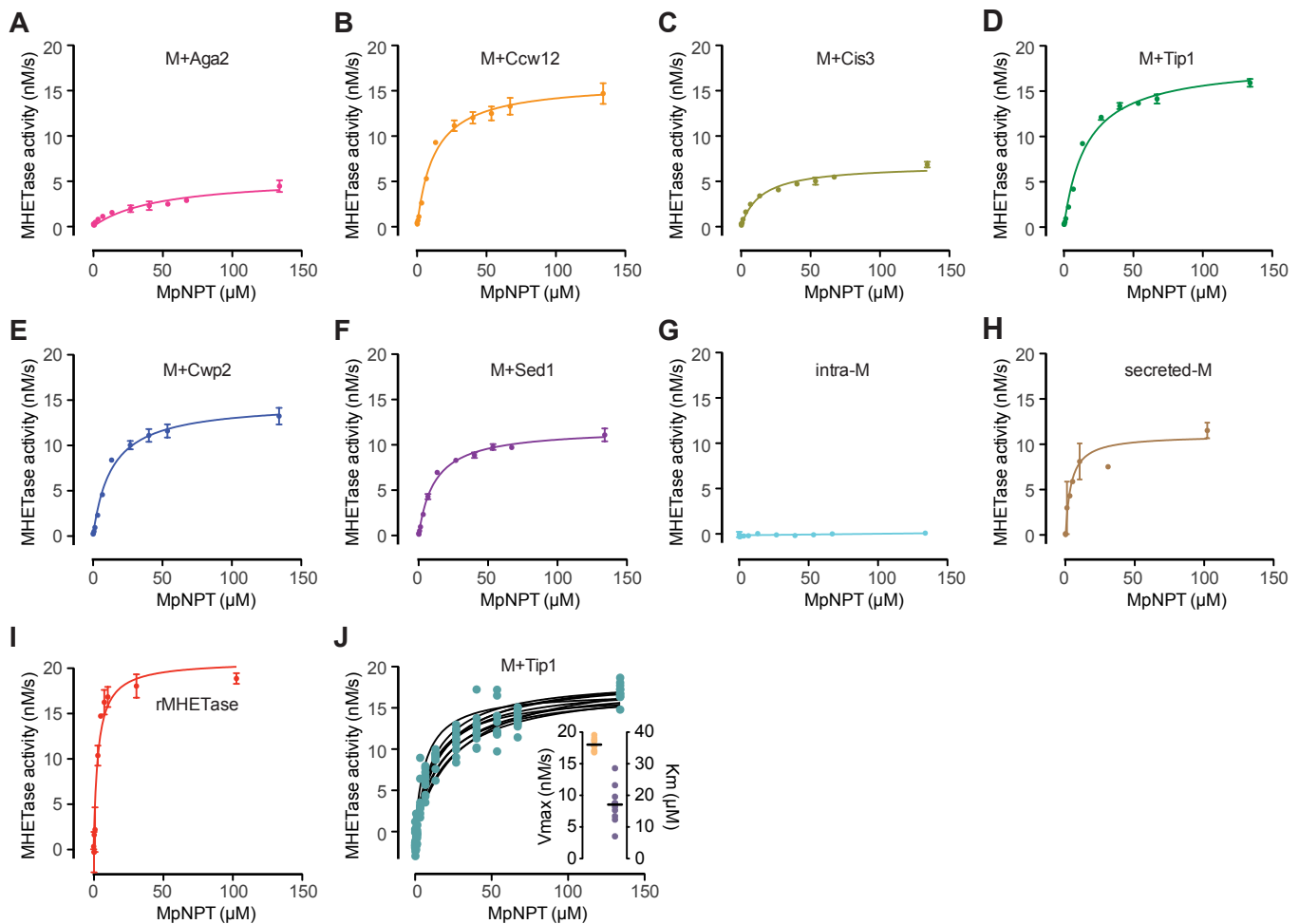
Figure 4. The MHETase whole-cell catalyst follows Michaelis-Menten kinetics. A through I. Michaelis-Menten plots for the MHETase chimeras and recombinant MHETase. For the displayed MHETase chimeras (A-G), cells were induced for 4 hours in YPD, rinsed twice and resuspended in 100mM phosphate buffer pH 7.5 prior to assaying MHETase activity by incubating with MpNPT at the indicated concentrations for 10 minutes at 24°C, followed by measuring absorbance at 405 nm. To allow comparison between samples of different cell density, MHETase activity was normalized to a cell density of 10^8 cells/ml. For the recombinant and secreted enzyme (H-I), assays were performed under the same buffer and temperature conditions in the presence of the indicated MpNPT concentrations. Michaelis-Menten curves were fitted to the data. **J.** To test for system robustness, seven biological replicates of the MHETase-Tip1 fusion were assayed in parallel. Michaelis-Menten curves were fitted to each independent replicate (black lines). Vmax and Km were calculated from the fitted curves (inset).
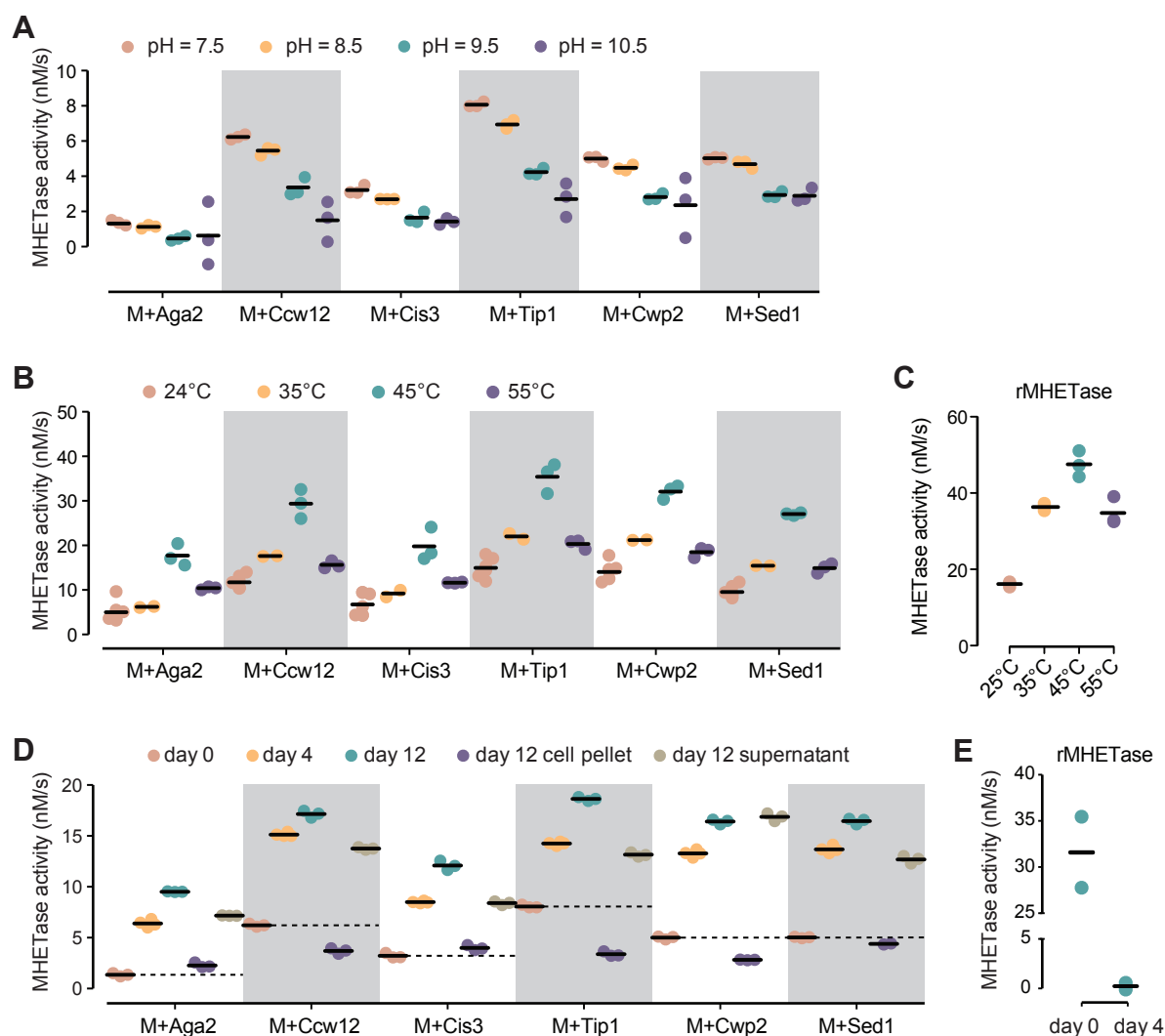
Figure 5. The MHETase whole-cell catalyst is stable to pH, temperature and time. A. MHETase activity at the indicated pH is plotted. MHETase activity was assayed with 26.8 μM MpNPT for 10 minutes at 24°C, followed by measuring absorbance at 405 nm. Activity was normalized to a cell density of 10^8 cell/ml. Horizontal bars indicate the means of the replicates (n = 3). **B.** MHETase activity at the indicated temperatures is plotted. n = 3. **C.** Activity of purified MHETase at different temperatures is plotted. Purified enzyme was diluted to 2 nM and and assayed with 50 μM MpNPT. n = 3. **D.** MHETase activity of the whole-cell catalysts was assayed at day 0, 4, and 12 during incubation at room temperature. At day 12, the cell suspension, cell pellet, and supernatants were assayed. MHETase activity was normalized to a cell density of 10^8 cell/ml at day 0. n = 3. **E.** Activity of purified MHETase over time. Purified enzyme was diluted to 2 nM and held at room temperature for 4 days. MHETase activity at day 4 was measured with 50 μM MpNPT at 25°C alongside a fresh aliquot of purified MHETase (day 0). n =2.